Thin Solid Films 750 (2022) 139183

Contents lists available at ScienceDirect

Thin Solid Films

journal homepage: www.elsevier.com/locate/tsf

Statistical modeling of epitaxial thin films of an intrinsic antiferromagnetic topological insulator

Rafaela F.S. Penacchio [a], Celso I. Fornari [b], Yorí G. Camillo [a], Philipp Kagerer [b], Sebastian Buchberger [b], Martin Kamp [c], Hendrik Bentmann [b], Friedrich Reinert [b], Sérgio L. Morelhão [a,*]

[a] Institute of Physics, University of São Paulo, São Paulo 05508-090, SP, Brazil
[b] Experimentelle Physik VII and Würzburg Dresden Cluster of Excellence ct.qmat, Fakultät für Physik und Astronomie, Universität Würzburg, Am Hubland, Würzburg, D-97074, Germany
[c] Physikalisches Institut and Röntgen-Center for Complex Material Systems (RCCM), Fakultätfür Physik und Astronomie, Universität Würzburg, Würzburg, D-97074, Germany

ARTICLE INFO

Keywords:
Magnetic topological insulators
Structure modeling
X-ray dynamical diffraction
Van der Waals epitaxy

ABSTRACT

Synthesis of materials demands structural analysis tools suited to the particularities of each system. Van der Waals (vdW) materials are fundamental in emerging technologies of spintronics and quantum information processing. In particular, topological insulators and, more recently, materials that allow the phenomenological exploration of the combination of non-trivial electronic band topology and magnetism. Weak vdW forces between atomic layers give rise to compositional fluctuations and structural disorder that are difficult to control, even in a typical topological insulator such as the binary compound Bi_2Te_3. The addition of a third element, as in $MnBi_2Te_4$, makes the epitaxy of these materials even more chaotic. In this work, statistical modeling of $Mn_xBi_2Te_{3+x}$ film structures is described. It allows the simulation of X-ray diffraction in disordered $MnBi_2Te_4$/Bi_2Te_3 heterostructures, a necessary step towards controlling the epitaxial growth of topological insulators with intrinsic magnetic properties. On top of this, the diffraction simulation method used here can be readily applied as a general tool in the field of materials design based on stacking of vdW bonded layers of distinct elements.

1. Introduction

Two-dimensional (2D) van der Waals (vdW) materials have experienced an explosive growth after graphene, and other families of 2D systems and block-layered bulk materials have been discovered [1–3]. The possibility of tuning their electronic properties via structural parameters make the layered vdW materials attractive from both fundamental and device engineering points of view. This field has become particularly interesting after the experimental discovery of three-dimensional (3D) topological insulators (TIs), having as prototypical the bismuth chalcogenide compounds [4–7]. To control the chemical potential of these compounds without using extrinsic doping, growth methods and properties of thin films have been investigated [8–11]. The weakness of vdW interlayer forces lead in general to systems undergoing drastic changes as a function of subtle variation in growth conditions. Finding controllable fabrication processes of such systems has proven challenging [12–14]. On top of this, the recently discovered intrinsic magnetic topological insulator $MnBi_2Te_4$ has added a another chapter to the phenomenological exploration of combining non-trivial electronic band topology and magnetism. Contrary to other attempts of breaking time-reversal symmetry by diluted doping of transition metals or rare-earth elements on 3D TIs [15–19], this material carries in its unit cell ordered layers of Mn atoms, providing a ferromagnetic ordering in the plane and a broad range of out-of-plane configurations depending on the stacking sequence [20,21]. Similar to other homologous series of bismuth chalcogenides [12,22,23], this compound is part of the $(MnBi_2Te_4)_n(Bi_2Te_3)_m$ series formed by stacking two fundamental building blocks that spans from Bi_2Te_3 ($n = 0$)—the archetypal of 3D TI without magnetic ordering—to the intrinsic antiferromagnetic $MnBi_2Te_4$ ($m = 0$), passing through an infinity of intermediary phases [24–27].

For the 3D non-magnetic TI, Bi_2Te_3, the unit cell is composed by

* Corresponding author.
E-mail address: morelhao@if.usp.br (S.L. Morelhão).

https://doi.org/10.1016/j.tsf.2022.139183
Received 31 August 2021; Received in revised form 17 March 2022; Accepted 17 March 2022
Available online 24 March 2022

Table 1
Sample labels, BEP ratio Φ_{Mn}, nominal film thickness t_f, substrate temperature during film growth T_{sub}, presence of 80 nm Te cap layer, $Mn_xBi_2Te_{3+x}$ film composition x, and methods of detecting film composition: shifting ΔQ_{L21} of the $L21$ peak position; or splitting ΔQ of the $L6$ peak, as detailed in Section 5.

Sample	Φ_{Mn}	t_f (nm)	T_{sub} (°C)	Te cap	x	ΔQ_{L21} (nm^{-1})	ΔQ (nm^{-1})
S06c	0.06	20	280	✓	0.73	−0.27	—
S07c	0.07	40	280	✓	0.86	−0.14	—
S11c	0.11	20	280	✓	0.80	−0.20	—
S075	0.075	20	280	×	0.70	—	1.5
S086	0.086	20	300	×	0.79	—	1.0
S102	0.102	20	280	×	> 0.80	—	0

stacking three quintuple layers (QLs). These QLs are fundamental building blocks always started and terminated in Te atoms as Te-Bi-Te-Bi-Te. The Te-Bi atoms are covalently bonded inside the QLs, while these blocks are coupled together along the [0001] direction due to weak vdW forces between the Te atoms in adjacent blocks. By inserting Mn in this structure, an extra MnTe double layer is formed inside the QL, leading to the existence of septuple layers (SLs) as Te-Bi-Te-Mn-Te-Bi-Te. The atomic Mn layer inside the SLs present a net out-of-plane magnetic moment, that is, the neighbor atoms are ferromagnetically coupled inside the layer. When stacked together, the SLs present antiferromagnetic (AFM) ordering. The intermediary phases are determined by the ratio of SLs and QLs, and present interesting AFM properties [28]. Besides the above mentioned magnetic properties of this series, an even richer interplay between topology and magnetism is expected in the 2D regime when reducing the number of stacked layers [1]. Such properties make this intrinsic magnetic TI highly attractive. However, a great challenge rising in this field is to control and understand the growth mechanisms of this compound in order to suppress the formation of structural defects and prepare perfectly ordered layers to explore the 3D to 2D transition.

Structural modeling via simulation of X-ray scattering and diffraction has well-established procedures for analyzing materials at nanometer and sub-nanometer length scales. In particular, procedures that have been widely used in thin-film-based device technologies where model refinement suites are available either for amorphous films with density fluctuation along the thickness [29] or crystalline films, such as those obtained in the epitaxy of semiconductor materials. In the case of TI compounds belonging to homologous series, model structures have to deal with statistical fluctuation of composition together with random stacking sequences of more than one type of building block. In other words, statistical models of disordered heterostructures are needed.

In this work, procedures to generate statistical structure models of TI compounds are described and implemented to simulate X-ray dynamical diffraction in thin films of $Mn_xBi_2Te_{3+x}$ (MBT) grown by molecular beam epitaxy on BaF_2 (111) single crystal substrates. The films are stacks of n vdW bounded $MnBi_2Te_4$ SLs where the occurrence of m Bi_2Te_3 QLs leads to films of composition $x = n/(n+m)$ and different disorder parameter, ranging from random to perfect periodic stacking sequences of atomic layers. Details in the X-ray reflectivity curves to quantify the composition and periodicity of the film are pointed out, leading to direct easy-to-access structural information for guiding the controlled growth of TI materials with optimized magnetic properties.

2. Materials and methods

Thin films of $(MnBi_2Te_4)_n(Bi_2Te_3)_m$ were grown on freshly cleaved BaF_2 (111) substrates using effusion cells charged with Bi_2Te_3 and phase pure MnTe as prepared by inorganic solid-state reactions [30]. The beam equivalent pressure (BEP) is monitored by an ion gauge before and after each growth. The manganese supply is defined by the ratio of the BEPs as $\Phi_{Mn} = BEP_{MnTe}/BEP_{Bi_2Te_3}$. During deposition, the background pressure stays below 5×10^{-6} Pa, against 7×10^{-9} Pa base pressure of the growth chamber. BaF_2 substrates were pre-heated at 350 °C for 10 min before starting deposition, and kept at 280 °C during deposition. All samples were prepared with a fixed $BEP_{Bi_2Te_3}$, resulting in a deposition rate of 0.02 Å/s for the Bi_2Te_3 cell. The Mn supply controlled through the MnTe effusion cell, providing $\Phi_{Mn} = 0.06$, 0.07, and 0.11 for samples labelled S06c, S07c, and S11c, respectively. These samples were covered with a 80 nm thick Te capping layer to avoid surface oxidation. Another set of samples, without the Te cap, was prepared within similar conditions: samples S075, S086, and S102 with $\Phi_{Mn} = 0.075$, 0.086, and 0.102, respectively. For sample S086, the substrate temperature was kept at 300 °C during deposition. Nominal thickness of the films is close to 20 nm, except in sample S07c where it is closer to 40 nm. Table 1 summarizes most characteristics of the samples.

XRD measurements were performed on a Bruker high resolution X-ray diffractometer equipped with Göbel mirror, Ge (220) monochromator, and Cu$K_{\alpha 1}$ radiation ($\lambda = 1.540562$ Å). Transmission electron microscopy (TEM) samples were prepared at the Wilhelm Conrad Röntgen Research Center for Complex Material System (RCCM) by using Ga^+ ion beam milling. Imaging was performed using an uncorrected FEI Titan 80–300 TEM, operating at 300 kV.

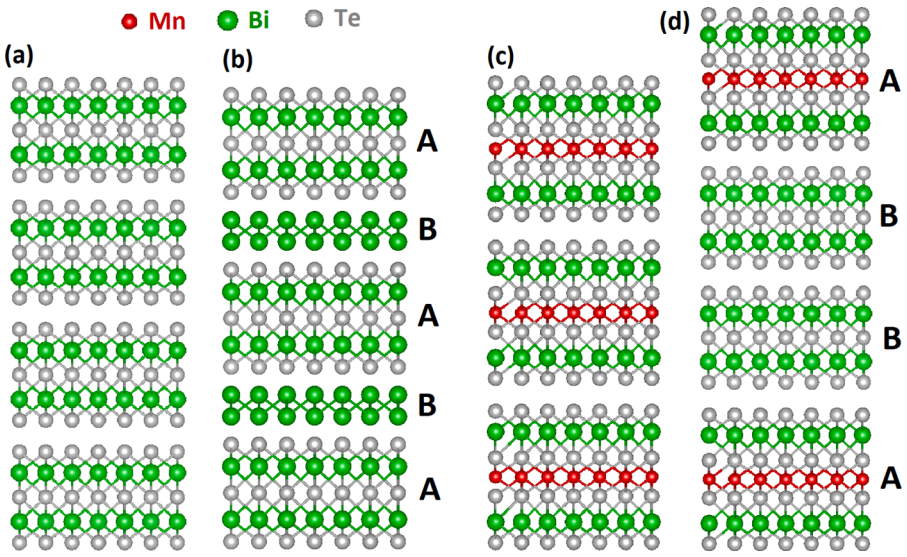

Fig. 1. Building blocks in $Bi_2Te_{3-\delta}$ and MBT epitaxial films. (a) Pure Bi_2Te_3 phase with no Te deficit ($\delta = 0$). (b) Bilayers of bismuth as in $(Bi_2Te_3)_n(Bi_2)_m = A_nB_m$ lead to films with Te defict $\delta = 3m/(n+m)$; main and secondary building blocks: A = Te-Bi-Te-Bi-Te and B = Bi-Bi. (c) Single $MnBi_2Te_4$ phase. (d) Mixing of phases $(MnBi_2Te_4)_n(Bi_2Te_3)_m = A_nB_m$ lead to $Mn_xBi_2Te_{3+x}$ films with composition $x = n/(n+m)$ or Mn deficit $\gamma = 1 - x = m/(n+m)$; main and secondary building blocks: A = Te-Bi-Te-Mn-Te-Bi-Te and B = Te-Bi-Te-Bi-Te.

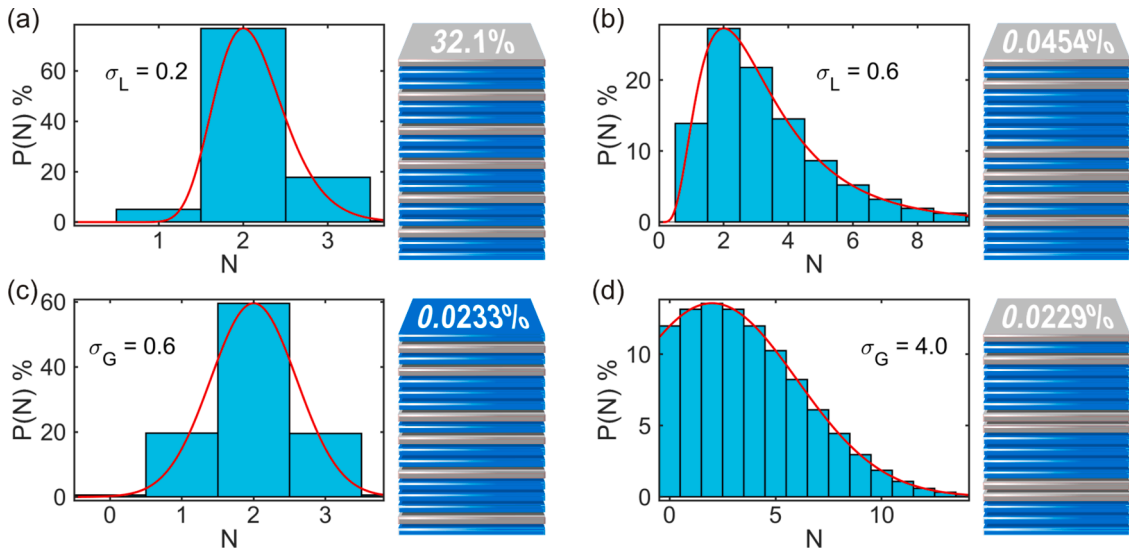

Fig. 2. Probability distribution functions $P(N)$, Eq. (1), for stacking sequences of N adjacent A blocks (blue layers) interleaved by B blocks (gray layers). (a,b) Using $p(z)$ (solid red lines) as lognormal functions of mode $N_0 = 2$ and standard deviations (a) $\sigma_L = 0.2$ and (b) $\sigma_L = 0.6$. (c,d) Using $p(z)$ (solid red lines) as Gaussian functions of mode $N_0 = 2$ and standard deviations (c) $\sigma_G = 0.6$ and (d) $\sigma_G = 4.0$. Examples of $A_{12}B_6$ film structures are shown aside the corresponding $P(N)$ function. Percentage values written at the top the films stand for their particular probability of occurrence, as computed on ensembles of one million models. (For interpretation of the references to color in this figure legend, the reader is referred to the web version of this article.)

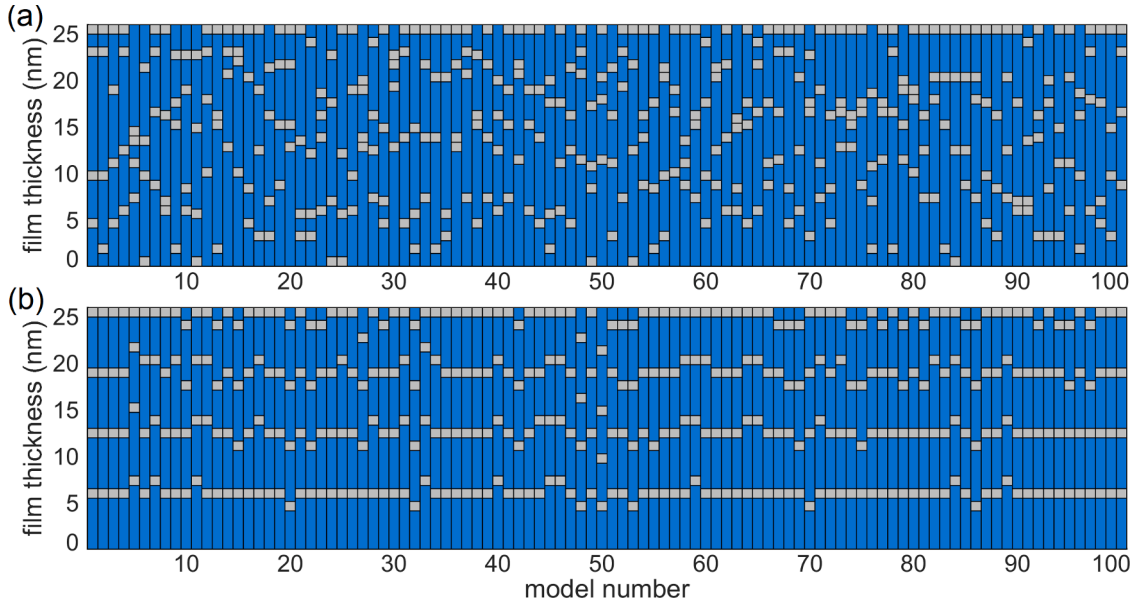

Fig. 3. Ensembles of hundred structure models for $A_{16}B_4$ films where $A = MnBi_2Te_4$ (blue, 1.36 nm thick) and $B = Bi_2Te_3$ (gray, 1.02 nm thick). Gaussian $p(z)$ function with (a) $\sigma_G = 4$ and (b) $\sigma_G = 0.4$ in Eq. (1). Total film thickness is 25.8 nm for all models. (For interpretation of the references to color in this figure legend, the reader is referred to the web version of this article.)

3. Structure models

A key point in vdW epitaxy is the weakness of interlayer forces. It favours, in principle, flexibilization of the lateral lattice matching requirements [31,32] at the same time that makes challenging the control of film composition and other lattice defects [13,33–35]. Modeling disordered heterostructures is a necessary step towards general procedures for structural analysis of materials based on vdW epitaxy. Composition fluctuation is related to the occurrence of distinct building blocks—sets of atomic monolayers sharing covalent bonds—randomly stacked along film thickness and bonded to each other by weak vdW forces. Fig. 1(a) and (b) show the building blocks that have been used for modeling $Bi_2Te_{3-\delta}$ films with deficit δ of tellurium [36], and in Fig. 1(d) and (c), the blocks that are used here for modeling the MBT films.

Accounting for the lack of perfect periodicity in films with composition fluctuation along thickness can be accomplished by correctly choosing a probability function to control the stacking sequences of two building blocks; the main block labeled A and the secondary one labeled B. To narrow the range of possibilities, two particular cases were considered. In one case, both types of building blocks can occur adjacently to each other, that is A:A and B:B pairs are possible. In the other case, adjacent blocks of the same kind occurs to A blocks only, that is no B:B pair in the film structure. Even in cases where the synthesis is aimed at materials with only the main block A, it is necessary to know how to evidence and quantify, if possible, the occurrence of the other block, block B, that is responsible for composition fluctuation. In more refined

Table 2
Atomic monolayers (ML) distances d in structure models of MBT films on BaF_2 (111) substrate. Building block A = Te(1)-Bi(1)-Te(2)-Mn(1)-Te(3)-Bi(2)-Te(4) and B = Te(1)-Bi(1)-Te(2)-Bi(2)-Te(3). Subtrate MLs along [111] direction: F(1)-Ba(1)-F(2), distances $d_{BaF} = 0.08949$ nm and $d_{FF} = 0.17898$ nm. In-plane lattice parameters: $a_A = 0.4334$ nm, $a_B = 0.4386$ nm, and $a_S = 0.4384$ nm. All d-values are from bulk [38,39].

Building block A ($MnBi_2Te_4$)		Building block B (Bi_2Te_3)	
MLs	d (nm)	MLs	d (nm)
Te(1)-Bi(1) and Bi(2)-Te(4)	0.17073	Te(1)-Bi(1) and Bi(2)-Te (3)	0.17434
Bi(1)-Te(2) and Te(3)-Bi(2)	0.21532	Bi(1)-Te(2) and Te(2)-Bi (2)	0.20331
Te(2)-Mn(1) and Mn(1)-Te (3)	0.15928	Te(3):Te(1) (B:B vdW gap)	0.26126
Te(4):Te(1) (A:A vdW gap)	0.27301	Te(1)-Te(1) → d_{QL}	1.01656
Te(1)-Te(1) → d_{SL}	1.36367	—	—

models, changes in the interlayer distances as a function of composition can be taken into account, as in the case of $Bi_2Te_{3-\delta}$ films [12,23]. However, in materials as the MBT epitaxial films [26], further improvement in film quality will be necessary before resolving the variations of interlayer distances with composition.

In structure models, the occurrence of N adjacent A blocks—without a B block in the middle—is given by the probability distribution function

$$P(N) = \Gamma \int_{N-1/2}^{N+1/2} p(z)\mathrm{d}z \tag{1}$$

where Γ is the normalization constant to ensure $\sum_{N=0}^{\infty} P(N) = 1$. For instance, $P(2) = 1$ provides periodic heterostructures of A:A:B sequences. For $P(2) < 1$, the probability of such periodic heterostructure within the ensemble of models having n repetitions of the A:A:B sequence is reduced to about $P(2)^n$. Examples of probability distribution functions and structure models they generate are displayed in Fig. 2. A criterion used here to chose the continuous function $p(z)$ was the occurrence of B:B pairs. In the case where there must be at least one A block in between two B blocks, as in B:A:B, $P(0) = 0$ even for highly disordered heterostructure. For this case, $p(z)$ was chosen to be a lognormal function with mode N_0 and standard deviation σ_L in log-scale, as shown in Fig. 2(a,b). To assure $P(0) = 0$ for all models, the small value of $p(z)$ in the range from $z = 0$ to $1/2$ is accounted for in $P(1) = \int_0^{3/2} p(z)\mathrm{d}z$. The lognormal function is suitable for modeling $Bi_2Te_{3-\delta}$ films where the bismuth bilayers, Fig. 1(b), are separated by at least one QL [36]. On the other hand, for the most general case of epitaxial film where both types of building blocks can form stacks of equal blocks, that is B:B pairs occurring with probability $P(0) > 0$, $p(z)$ was chosen to be a Gaussian function of mode N_0 and standard deviation σ_G, as shown in Fig. 2(c,d). In the last example, Fig. 2(d), $P(0) \simeq 12\%$ is a value comparable to the probability of the mode, $P(2) \simeq 14\%$, favouring a few B:B pairs to occur in the model structures, as seen for instance in the $A_{12}B_6$ film scheme aside the $P(N)$ function. Stacks of more than two B blocks is also possible, such as B:B: …B with j adjacent blocks, but the probability for its occurrence decreases to about $P(0)^{j-1}$. A given stacking sequence within an ensemble of disordered heterostructures can have a very low probability, as computed for the particular $A_{12}B_6$ films in Fig. 2.

4. X-ray diffraction simulation

For a given probability function and film composition, hundreds of structure models are generated with constant numbers of both A and B blocks, as graphically illustrated in Fig. 3. Such ensemble of models represents possible statistical fluctuation within film domains distributed over the sample area. X-ray reflectivity of each model is calculated by adding up reflection and transmission coefficients of the successive layers along film thickness. If $r_{X,Y}$ and $t_{X,Y}$ stand for reflection and transmission coefficients of generic X and Y layers, the coefficients of the combined Y:X layer with X on top of layer Y are calculated according to Morelhão et al. [36]

$$\begin{aligned} r_{YX} &= r_X + r_Y \frac{t_X t_X\, e^{2i\varphi}}{1 - \bar{r}_X r_Y\, e^{2i\varphi}}, \\ \bar{r}_{YX} &= \bar{r}_Y + \bar{r}_X \frac{t_Y t_Y\, e^{2i\varphi}}{1 - \bar{r}_X r_Y\, e^{2i\varphi}}, \quad \text{and} \\ t_{YX} &= \frac{t_X t_Y\, e^{i\varphi}}{1 - \bar{r}_X r_Y\, e^{2i\varphi}}. \end{aligned} \tag{2}$$

$\varphi = -\frac{1}{2}Qd$ is the phase delay every time the X-ray wave of wavelength λ crosses the interlayer distance d between the X and Y layers, and $Q = (4\pi/\lambda)\sin\theta$ is the modulus of the scattering vector perpendicular to film

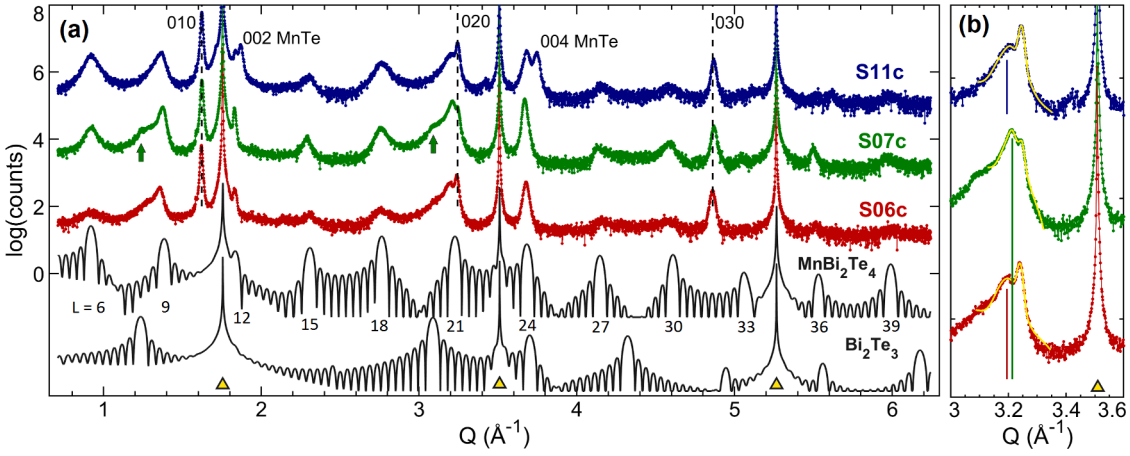

Fig. 4. (a) Q-scans along the surface normal direction in epitaxial MBT films on BaF_2 (111) substrate. $Q = (4\pi/\lambda)\sin\theta$. Sample labels (see Table 1) are indicated aside each experimental scan. Sharp-high intensity peaks stand for 111, 222, and 333 reflections of the substrate lattice (triangles at the bottom). The 010, 020, and 030 reflections (dashed lines) from a hexagonal Te phase [41] are originated by the Te protective capping layer, while the 002 and 004 reflection indexes refer to a hexagonal MnTe phase [42] observed in the sample S11c only. Broad peaks are 00L reflections (L = 6, 9,… 39) from MBT films. Contributions from Bi_2Te_3 layers are pointed out by arrows. Simulated curves for MBT and Bi_2Te_3 single phase 13 nm thick films are shown at the bottom (out of vertical scale) as reference for peak positions. (b) Zooming of experimental profiles around film L21 peak and substrate 222 reflection. Q positions (vertical lines) of the L21 peaks obtained by line profile fitting (yellow lines) are indicated: $Q_{21}^{S06c} = 3.201$ Å^{-1}, $Q_{21}^{S07c} = 3.214$ Å^{-1}, and $Q_{21}^{S11c} = 3.208$ Å^{-1} for samples S06c, S07c, and S11c, respectively. (For interpretation of the references to color in this figure legend, the reader is referred to the web version of this article.)

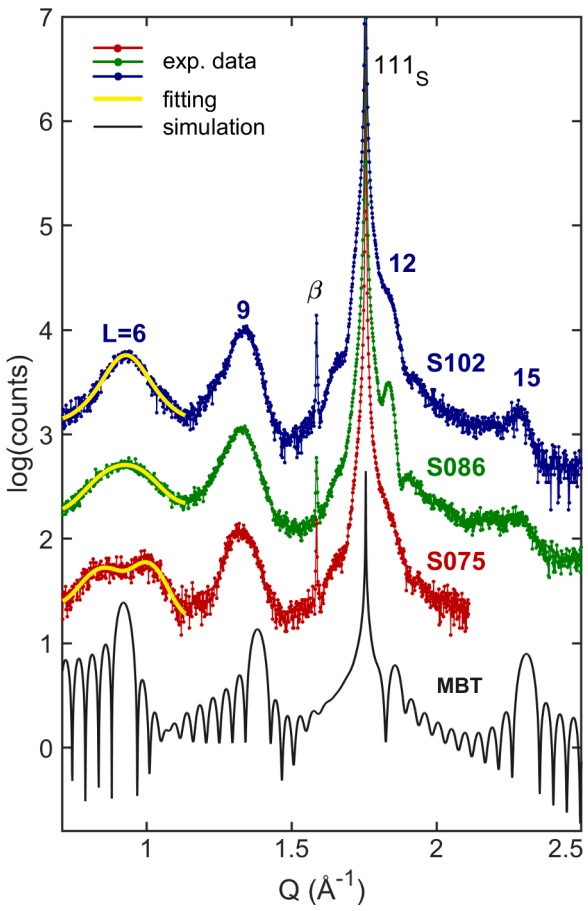

Fig. 5. Q-scans along the surface normal direction in epitaxial MBT films on BaF_2 (111) substrate. $Q = (4\pi/\lambda)\sin\theta$. Sample labels (see Table 1) are indicated aside each experimental scan (lines with dots). Film 00L reflections with $L = 6$, 9, 12, and 15 are visible, as well as the 111 substrate reflection. Simulated curve for a 13.8 nm thick MBT film is shown at the bottom (out of vertical scale) as reference for peak positions. A sharp peak (label β) from CuK_β radiation is seen in the experimental scans. Line profile fitting (yellow lines) by two gaussians of the diffraction peak L6 provide splitting values of $\Delta Q = 0.15$ Å^{-1}, 0.10 Å^{-1}, and null for samples S075, S086, and S102, respectively. (For interpretation of the references to color in this figure legend, the reader is referred to the web version of this article.)

thickness for an incidence angle θ. In general, reflection coefficients are different when the X-ray impinges from the top, coefficients r_X, r_Y, and r_{YX}, or from the bottom, coefficients $\bar{r}_X$, $\bar{r}_Y$, and $\bar{r}_{YX}$.

Eq. (2) are used recursively, starting from the atomic monolayers within the building blocks A and B, whose interlayer distances are given in Table 2. For an atomic monolayer, $r_X = \bar{r}_X = -i\Gamma\sum_a \eta_a f_a(Q,E)$ and $t_X = 1 + i\Gamma\sum_a \eta_a f_a(0,E)$ where η_a is the area density of atoms a in the monolayer plane and $f_a(Q,E) = f_a^0(Q) + f_a'(E) + if_a''(E)$ are their atomic scattering factors with resonant amplitudes for X-ray photons of energy E, see Appendix A.3. The parameter $\Gamma = r_e\lambda C/\sin\theta$ arises from the scattering and photoelectric absorption cross sections, and it is very small due to the value of electron radius $r_e = 2.818 \times 10^{-5}$ Å. The $\sin\theta$ takes into account area variation of the beam footprint at the sample surface, and the polarization term C is always equal to 1 for t_X, as well as in r_X when using linearly polarized X-rays (most synchrotron facilities) [37]. For accurate curve fitting purposes with unpolarized X-rays, take $C^2 = \frac{1}{2}(1+\cos^2 2\theta)$ in r_X. Throughout this work, $C = 1$ is considered for the sake of simplicity.

After calculating the reflection coefficients r_A and r_B of the A and B building blocks, the reflection coefficients of any sequence of blocks such as A:A:B:A:A:B follows straightforward from Eq. (2) by replacing X and Y layers as follow:

$$\begin{array}{rcl} (Y=A, X=A) & \rightarrow & r_{AA}\,, \\ (Y=AA, X=B) & \rightarrow & r_{AAB}\,, \quad \text{and} \\ (Y=AAB, X=AAB) & \rightarrow & r_{AABAAB}\,. \end{array} \tag{3}$$

The A:A and B:B vdW gap distances are given in Table 2, and the mean value of 0.26713 nm has been used for the A:B vdW gap. In most cases, it is necessary to consider the presence of the perfect and thick substrate lattice underneath the film. As detailed elsewhere [36], Eq. (2) also provides the dynamical diffraction solution in specular reflection geometry where refraction, rescattering, and photoelectric absorption are taken into account—the impact of the rescattering phenomenon on the diffracted intensities can be figured out by suppressing the term $\bar{r}_X r_Y e^{2i\varphi}$ in the denominator of the coefficients in Eq. (2). The reflection coefficient r_S, obtained from Eq. (2), for a thick substrate can be included when simulating the X-ray reflectivity curve $R(\theta)$ for a given model by repeating one more step of the recursive procedure in which

$$(Y=S, X=AABAAB) \rightarrow r_{SAABAAB}\,.$$

It provides $R(\theta) = |r_{SAABAAB}|^2$ as the reflectivity curve of the particular example of model in Eq. (3) grown on top of a single crystal substrate undergoing dynamical diffraction.

5. Results and discussions

Experimental and simulated long-range Q-scans along the surface normal direction are shown in Fig. 4. Diffraction peaks of epitaxial MBT films are clearly identified by comparing with the simulated ones. Traces of Bi_2Te_3 layers are seen in sample S07c (arrows) near peaks $L9$ and $L21$ of the MBT film. Besides film and substrate reflections, there are also diffraction peaks of 010, 020, and 030 reflections from the protective Te capping layer, and two diffraction peaks from a MnTe phase in the S11c film grown under higher Mn supply. The presence of MnTe layers epitaxially oriented with the substrate lattice have already been observed, as well as the formation of multiple MnTe layers inside the $MnBi_2Te_4$ blocks, given rise to blocks composed of 9, 11 or 13 layers [40]. The presence of MnTe clusters perturb locally the magnetic order of the sample and must be avoided.

Fig. 5 shows Q-scans for the samples without the Te capping layer. No signal from the 002 MnTe reflection can be identified at the right side of the MBT $L12$ peak, even in the case of sample S102 with Mn supply $\Phi_{Mn} = 0.102$ that is close to $\Phi_{Mn} = 0.11$ used for preparing sample S11c (Fig. 4). There are other features evidenced by these intensity curves. As the Mn supply increases, peak $L6$ becomes narrower and peak $L9$ moves slightly towards the expected position of the pure phase. By fitting the line profile of peak $L6$ with two gaussians, they appears set apart by $\Delta Q = 0.15$ Å^{-1} and 0.10 Å^{-1} in the samples S075 and S086, respectively. In the S102 sample, no separation of the gaussians is detected. To clearly understand such features, XRD simulation becomes crucial. Structure models of MBT films based on two building blocks, as depicted in Fig. 1(d), are supported by TEM images as the one in Fig. 6 where only $MnBi_2Te_4$ septuple layers (SLs) and Bi_2Te_3 quintuple layers (QLs) have been observed [26]. Bismuth bilayers owing to the deficit of tellurium have been suppressed, probably due to the extra amount of Te from the MnTe source.

Simulated Q-scans in disordered $(MnBi_2Te_4)_n$ $(Bi_2Te_3)_m$ films as a function of the Mn deficit $\gamma = m/(n+m)$ are shown in Fig. 7; simulation in grazing incidence region, $Q < 0.3$ Å^{-1}, is detailed in Appendix A.1. For a given degree of disorder, the simulated curves reveal that well visible diffraction peaks as $L6$ and $L18$ undergo a splitting into two superlattice satellite peaks set aparted by a ΔQ value nearly proportional to the content of QLs (Bi_2Te_3 blocks) or Mn deficit. Most satellite peaks vanish as the disorder parameter σ_G increases, as better seen in Fig. 8. But, the splitting of the $L6$, $L18$, and $L30$ peaks remain measurable even in films where the QLs are distributed with high degree of disorder. It

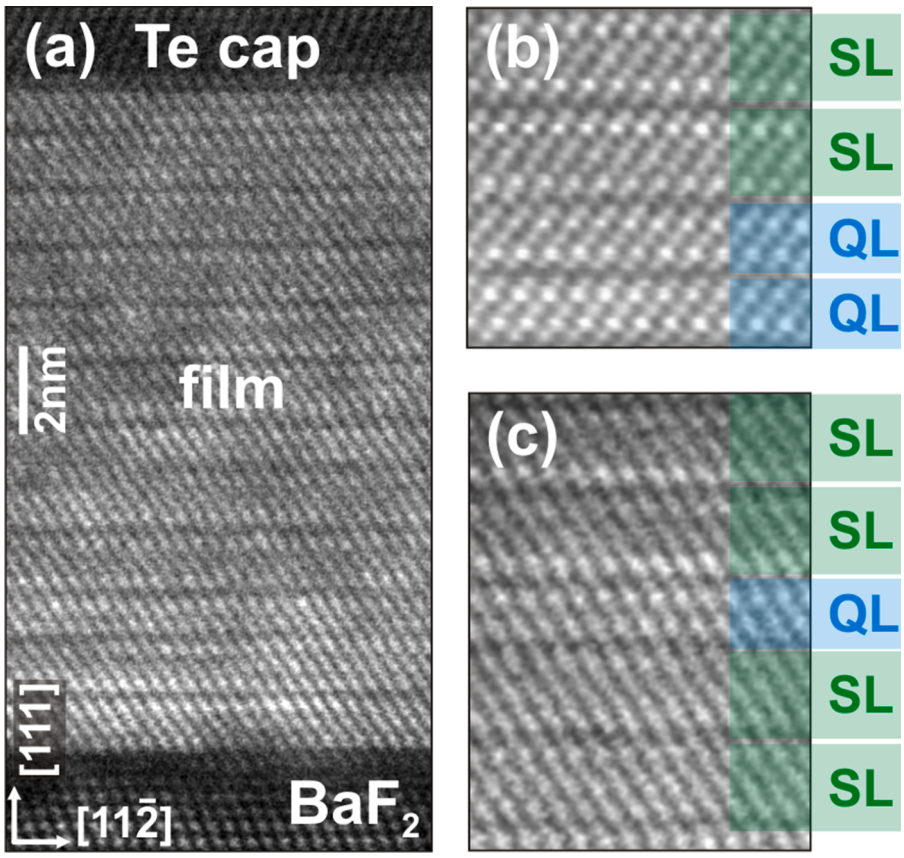

Fig. 6. Scanning transmission electron microscopy cross-sectional images of a 15 nm thick MBT film capped with Te. (a) Cross-sectional overview image showing the BaF_2 substrate, the epitaxial film, and the Te protective capping layer. (b,c) Detailed views of the film structure showing the coexistence of septuple layers (SLs) and quintuple layers (QLs).

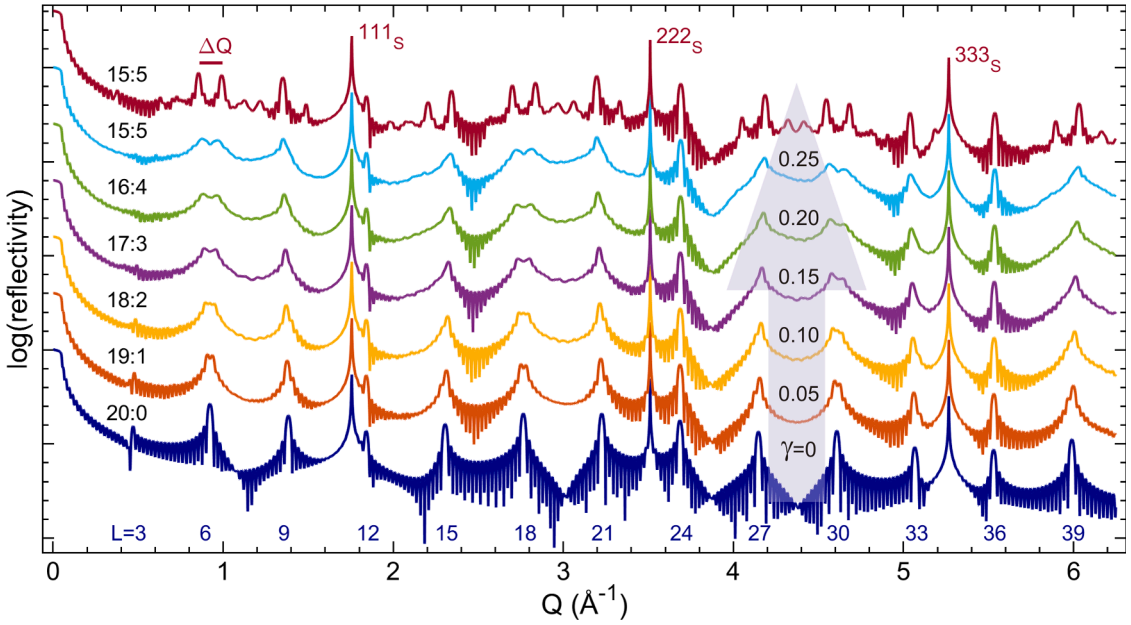

Fig. 7. Simulated Q-scans in epitaxial $(MnBi_2Te_4)_n(Bi_2Te_3)_m$ films on BaF_2 (111) substrate as a function of compositon n:m. Structure models of disordered building blocks according to Eq. (1) with $\sigma_G = 10$ ($\sigma_G = 0.1$ for the top curve only). L index of 00L reflections in single phase epitaxial MBT films are indicated at the bottom, and substrate reflection at the top. ΔQ splitting of the $L6$ peak is proportional to the Mn deficit $\gamma = m/(n+m)$, as well as of the $L18$ and $L30$ peaks.

also occurs in much thicker films, as demonstrated for a 510 nm thick film in Appendix A.1. Within the approximation of stable interlayer distances summarized in Table 2, the films have thickness $T = n\,d_{SL} + m\,d_{QL}$, and mean superlattice period $\langle D\rangle = T/m$ where $d_{SL} = 1.36367$ nm and $d_{QL} = 1.01656$ nm (Table 2). It provides satellite reflections set aparted by

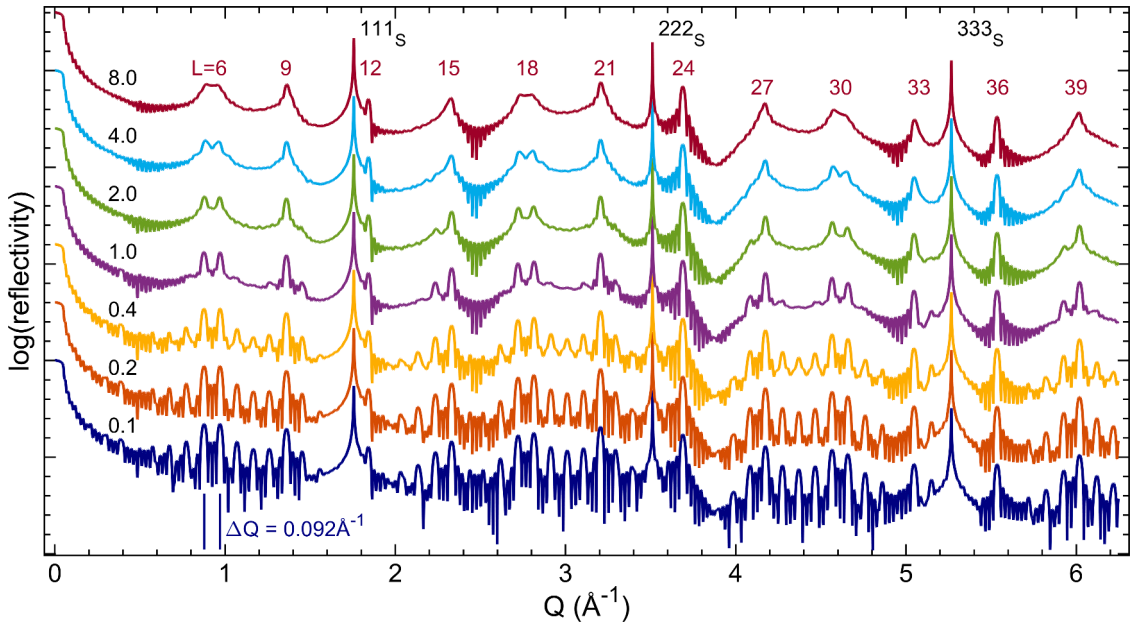

Fig. 8. Simulated Q-scans in epitaxial $(MnBi_2Te_4)_{16}(Bi_2Te_3)_4$ films on BaF_2 (111) substrate as a function of $\sigma_G = 0.1, 0.2, \ldots, 8$ in Eq. (1). Each simulation corresponds to the average curve calculated over an ensemble of 100 models of disordered heterostructures, such as those in Fig. 3.

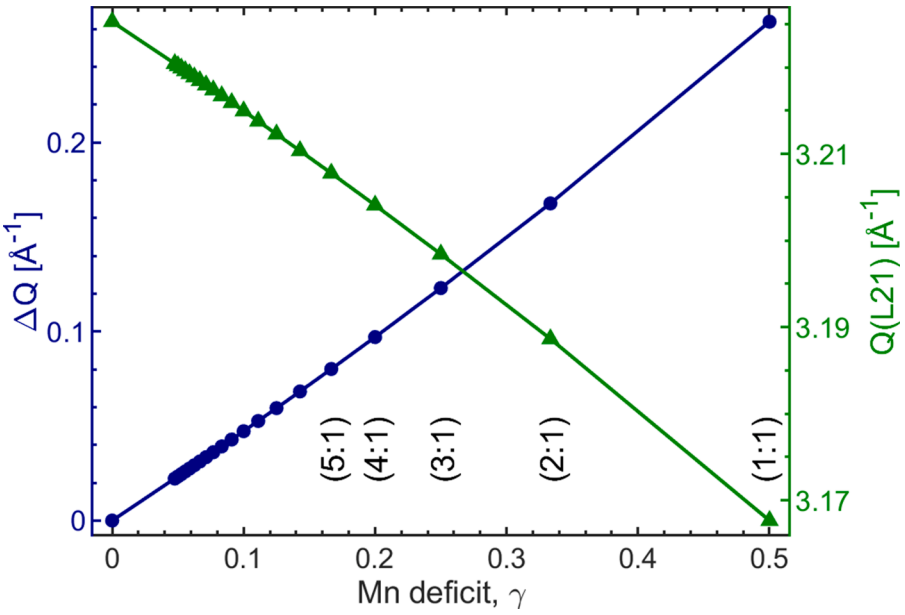

Fig. 9. Structural parameters accessible from X-ray reflectivity curves as a function of the Mn deficit γ in MBT films. ΔQ (blue solid line and circles, left axis) stands for the separation between adjacent superlattice peaks, Eq. (4), that are well visible as a splitting of the $L6$ and $L18$ peaks. $Q(L21)$ (green solid line and triangles, right axis) is the $L21$ peak position given by Eq. (5). $\gamma = m/(n+m)$ for a film with composition n:m as indicated near a few points. (For interpretation of the references to color in this figure legend, the reader is referred to the web version of this article.)

$$\Delta Q(\gamma) = \frac{2\pi}{\langle D\rangle} = \frac{2\pi m}{n d_{SL} + m d_{QL}} = \frac{2\pi\gamma}{d_{SL} - \gamma(d_{SL} - d_{QL})} \approx \frac{2\pi}{d_{SL}}\gamma\,. \tag{4}$$

The Mn deficit γ also shifts the $L21$ peak position. In $MnBi_2Te_4$ film, the lattice parameter $c = 3d_{SL}$, $Q = 2\pi L/c$, and hence for $L = 21$, $Q_{21} = 2\pi/\langle d\rangle_0$ as $\langle d\rangle_0 = d_{SL}/7$. In the case of $(MnBi_2Te_4)_n(Bi_2Te_3)_m$ films, the mean atomic interlayer distance is $\langle d\rangle = T/(7n+5m)$ where $7n+5m$ corresponds to the total number of atomic monolayers stacked along the film thickness. It leads to

$$Q_{21}(\gamma) = \frac{2\pi}{\langle d\rangle} = \frac{2\pi(7-2\gamma)}{d_{SL} - \gamma(d_{SL} - d_{QL})} \approx \frac{2\pi}{\langle d\rangle_0} + \frac{2\pi}{\langle d\rangle_0}\left(\frac{5}{7} - \frac{d_{QL}}{d_{SL}}\right)\gamma\,. \tag{5}$$

The linear behavior of ΔQ and Q_{21} as function of γ are shown in Fig. 9. For low Mn deficit ($\gamma \lesssim 0.25$), the splitting can be taken as $\Delta Q \approx 0.46\,\gamma\,[\text{Å}^{-1}]$, while the shift in the $L21$ peak position is $\Delta Q_{21}(\gamma) = Q_{21}(\gamma) - 2\pi/\langle d\rangle_0 \approx -0.10\,\gamma\,[\text{Å}^{-1}]$.

By using the substrate 222 reflection at $Q = 3.5105(\pm 0.0001)$ Å^{-1} as reference, the expected $L21$ peak position is at $Q_{21}(0) = 2\pi/\langle d\rangle_0 = 3.2253$ Å^{-1} for unstrained non-tilted epitaxial films with no Mn deficit. In Fig. 4(b), the experimental $L21$ peaks have been observed at sligthly different positions, implying in $\Delta Q_{21}^{S06c} = Q_{21}^{S06c} - Q_{21}(0) = -0.027$ Å^{-1}, $\Delta Q_{21}^{S07c} = -0.014$ Å^{-1}, and $\Delta Q_{21}^{S11c} = -0.020$ Å^{-1}. According to Eq. (5), the analyzed films have compositions $x = 0.73$, 0.86, and 0.80, respectively. However, these values are reliable as far as the interlayer distances have no dependence with composition, disorder, and film thickness. In highly disordered heterostrucutres, peak broadening is observed instead of peak splitting into superlattice satellite peaks. The X-ray reflectivity simulations in Figs. 7 and 8 clearly show

that peaks susceptible to composition are much broader than other peaks, such as the $L24$ peak that has presented a nearly constant width as a function of composition and heterostructure disorder. Therefore, $L6$ peak significantly broader than $L24$ peak can be taken as another evidence, although qualitative, of Mn deficit and disorder in the films. For the sake of comparison, the $L6$ peaks in the S06c, S07c, and S11c samples have width (fwhm) around $w_{L6} \approx 0.067$ Å^{-1}, against nearly half of this value for the $L24$ peak.

Invariance of $L24$ peak width with composition and disorder implies that their widths $w_{24}^{S06c} = 0.0315$ Å^{-1}, $w_{24}^{S07c} = 0.0260$ Å^{-1}, and $w_{24}S11c = 0.0386$ Å^{-1} from the experimental Q-scans, Fig. 4(a), can be used as a measure of the longitudinal coherence lengths of 20.0(±1.0) nm, 24.2(±1.2) nm, and 16.3(±0.7) nm, respectively. For samples S06c and S11c, these lengths are close to the nominal thickness of 20 nm. But for sample S07c, the coherence length is smaller than the nominal thickness of 40 nm, probably indicating to structural defects unaccounted for in the X-ray diffraction simulation. Main peaks of the Bi_2Te_3 phase are clearly observed in the Q-scan of sample S07c, as pointed out by arrows in Fig. 4 (a). It means that segregation of phases has occurred in this film, which can in part justify a longitudinal coherence length smaller than the total film thickness and also corroborate to MBT phase with composition closer to $x = 1$.

Although vdW epitaxy can take place on substrates with relatively large lateral lattice mismatch [11,43–45], it has been demonstrated in Bi_2Te_3 (001) films on BaF_2(111) that even mismatch as small as 0.02% can drastically impact the lateral lattice coherence length, or the lateral size of crystalline domains [13,46]. In $MnBi_2Te_4$ (001) films on BaF_2 (111) the lattice mismatch $|\Delta a/a| = |a_A - a_s|/a_S$ is much bigger, of about 1.1%. If the amount ε of lattice misfit that can be elastically accommodated remains within the same order of magnitude, around 5×10^{-3} as observed in Bi_2Te_3 films, the lateral coherence length in $MnBi_2Te_4$ films is probably smaller than 27 nm ($\approx \frac{a_s}{\varepsilon + |\Delta a/a|}$) [13]. An indirect evidence of shorter in-plane coherence length is the absence of thickness fringes around peak $L24$, as smaller domains can lead to more irregular film surfaces smearing out the fringes. The necessary thickness fluctuation for eliminating fringes around the $L24$ peak is discussed in Appendix A.2.

In the case of samples S075, S086, and S102 with exposed films—no cap layers—, the splitting of peak $L6$ in two superlattice peaks as a function of the Mn supply is better evidenced, Fig. 5. By using Eq. (4) and the measured values of ΔQ, the Te deficit of $\gamma = 0.30$ and 0.21 are obtained for samples S075 and S086, respectively. Both sets of samples, the capped and not capped ones, are indicating that to prevent the formation of undesired MnTe layers by limiting the Mn supply to about $\Phi_{Mn} = 0.1$, films with composition close to $Mn_{0.8}Bi_2Te_{3.8}$ are obtained. This value of $x \simeq 0.8$ also corresponds to a limit value of composition detection capability by X-ray diffraction regarding the actual quality of the epitaxial MBT films.

Results from the statistical modeling presented in this work can be useful to describe other experimental data available in the literature. In particular, the predicted ΔQ splitting of the $L6$, $L18$, and $L30$ peaks as a function of Mn deficit γ, Fig. 7. It has been observed in a series of uncapped epitaxial MBT films growth by MBE on Al_2O_3 (001) substrates where the Mn deficit varies systematically from $\gamma \simeq 0$ to 0.5, that is from a $MnBi_2Te_4$ to $MnBi_4Te_7$ film structure [27].

6. Conclusion

X-ray diffraction simulation in $(MnBi_2Te_4)_n$ $(Bi_2Te_3)_m$ structure models as a function of composition and disorder has pointed out a few features that can be promptly exploited in structural analysis of MBT films obtained by molecular beam epitaxy. There are diffraction peaks that split up into superlattice satellites peaks whose separation is directly proportional to the Mn deficit γ, and another peak whose position can be used to measure the value of γ. On top of this, there are peaks with line profiles independent of composition and disorder, and can lead to a measure of the longitudinal coherence length. The models used to demonstrate these features were based on a Gaussian probability distribution of the two building blocks present in the n:m heterostructures. The experimental results showed that increasing the Mn supply provides just a little improvement in composition, with x from around 0.7 to 0.8. The MBT phase with highest composition, $x = 0.86$, was observed in the thicker film where some phase segregation is also observed.

Credit author statement

R.F.S.P.: Writing computer codes, Simulated and experimental data curation, Writing original draft. **C.I.F.**: Materials synthesis, Experimental data curation, Writing original draft. **Y.G.C.**: Simulated and experimental data curation, Writing original draft. **P.K.**: Materials synthesis, Experimental data aquisition. **S.B.**: Materials synthesis, Experimental data aquisition. **M.K.**: Experimental data aquisition. **H.B.**: conceptualization, Materials synthesis **F.R.**: Conceptualization, Materials synthesis, Supervision. **S.L.M.**: Conceptualization of structural modeling, Supervision, Writing original draft, Writing review & editing.

Declaration of Competing Interest

The authors declare that they have no known competing financial interests or personal relationships that could have appeared to influence the work reported in this paper.

Acknowledgments

We acknowledge financial support from the DFG through no. SFB1170 “Tocotronics” (Projects A01 and C06), No. SFB1143 “Correlated Magnetism,” and the Würzburg-Dresden Cluster of Excellence on Complexity and Topology in Quantum Matter ct.qmat (EXC 2147, Project no. 390858490) and from the BMBF (Project no. 05K19WW2). R. F.S.P., Y.G.C., and S.L.M. acknowledges financial support from FAPESP (Grant no. 2019/01946-1, 2021/01004-6), CNPq (Grant no. 310432/2020-0), and CAPES (finance code 001).

Appendix A

A1. Grazing incidence X-ray reflectometry and thick films

The set of recursive equations used for X-ray diffraction simulation in this work, Eq. (4) of the main text, is also valid at low Q in grazing incidence specular reflection geometries [29,47,48]. In Fig. A1, it is demonstrated for $(MnBi_2Te_4)_n(Bi_2Te_3)_m$ heterostructures as a function of degree of disorder and composition. Using ensemble of model structures of disordered heterostructure is a method quite limited for X-ray reflectivity simulation at grazing incidence angles. In actual films, this method of adding diffracted intensities from many statistically equivalent models is accurate for films with large crystallographic domains where interference effects between laterally adjacent domains can be neglected. The method become more reliable at wide angles where these interference effects are minimized. A more detailed discussion on this subject can be found elsewhere [48]. This set of recursive equations that become very suitable for layered materials has emerged within the vast effort to advance X-ray diffraction methods for

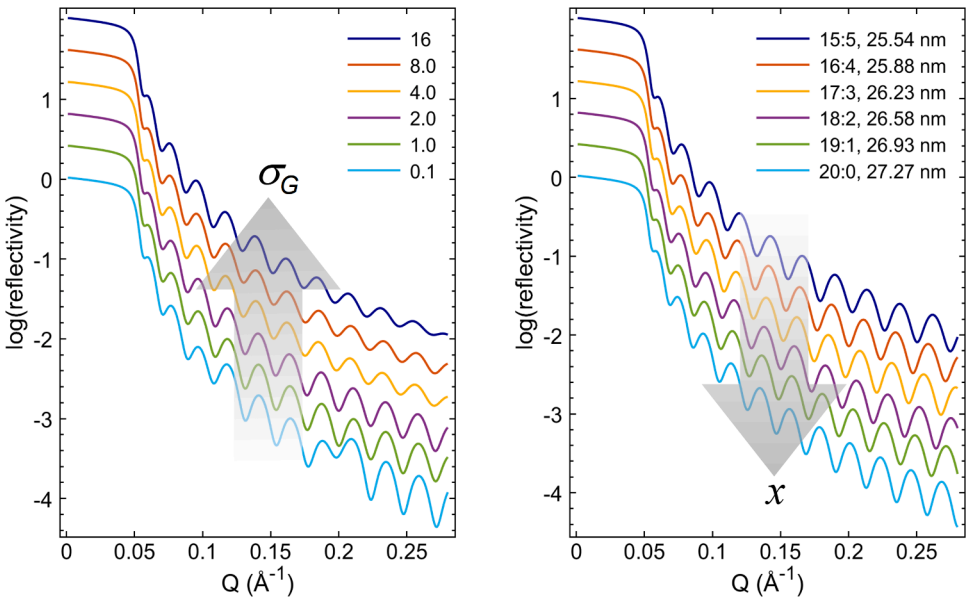

Fig. A1. X-ray reflectivity simulation in $(MnBi_2Te_4)_n(Bi_2Te_3)_m$ heterostructures on BaF_2 (001) at grazing incidence angles, $\theta < 5^\circ$ for CuK_α radiation. Left panel, 16:4 heterostructures as a function of the disorder parameter σ_G, Eq. (1), varying from 0.1 to 16 as indicated. Right panel, *n*:*m* heterostructures as a function of composition $x = n/(n+m)$ and constant degree of disorder $\sigma_G = 1$. Total film thickness $T = n\,d_{SL} + m\,d_{QL}$ is also indicated where $d_{SL} = 1.364$ nm and $d_{QL} = 1.0165$ nm (Table 2).

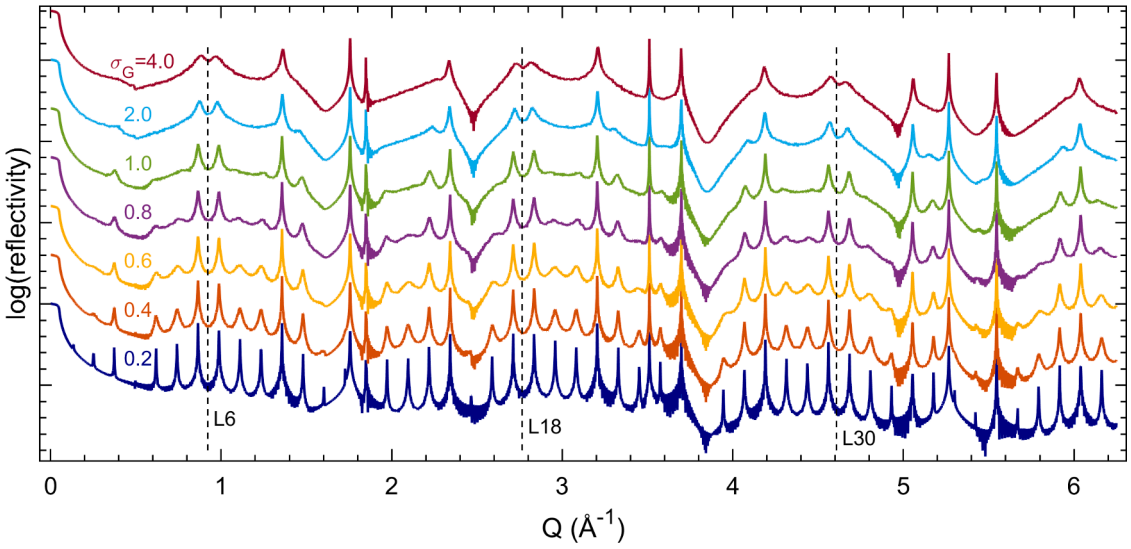

Fig. A2. Simulated *Q*-scans for 510 nm thick $Mn_{0.75}Bi_2Te_{3.75}$ films on BaF_2 (111) substrates as a function of the disorder parameter $\sigma_G = 0.2, 0.4, \ldots, 4$ in Eq. (1). These films stand for disordered heterostructures of 300 SLs and 100 QLs. Atomic resonant amplitudes were considered for Cu$K_{\alpha 1}$ radiation. Positions of *L*6, *L*18, and *L*30 $MnBi_2Te_4$ diffraction peaks are indicated (vertical dashed lines).

analyzing relevant materials, ranging from nanostructured devices to biological tissues [37,46,49–54].

Although the recursive series for X-ray diffraction simulation has been applied for thin films only, it is also suitable for thick films and semi-infinte crystals (substrate). Splitting of $MnBi_2Te_4$ diffraction peaks into satellites peaks as the deficit of Mn increases, and prevalence of visibility of the *L*6, *L*18, and *L*30 peak splitting even in disordered heterostrucutes is shown in Fig. A2 for 510 nm thick $(MnBi_2Te_4)_{300}(Bi_2Te_3)_{100}$ films.

A2. Thickness fluctuation

The quality of epitaxial films is strongly dictated by lattice matching. In van der Waals (vdW) epitaxy where week interlayer forces are responsible for the film structure along the growth direction, films of good quality can be achieved even in cases where there are misfits of a few percents [31–35]. However, the misfit between film and substrate in-plane lattice parameters impacts the lateral lattice coherence length, that is the size of perfect crystallographic domains [13]. Small uncorrelated domains lead to thickness fluctuation that can be inferred by the absence of thickness fringes in the reflectivity curves. At grazing angles there is the problem that severe thickness inhomogeneity can compromise data analysis. Fortunately X-ray diffraction simulation of long *Q* scans in $(MnBi_2Te_4)_n(Bi_2Te_3)_m$ heterostructures have revealed a few reflections, such as the L24, around which thickness fringes are visible regardless disorder and composition.

To estimate the amount of thickness fluctuation necessary for eliminating the fringes around the L24 peak, a weight function

$$W(N) = \int_N^{N+1} L(x)dx\,, \tag{A.1}$$

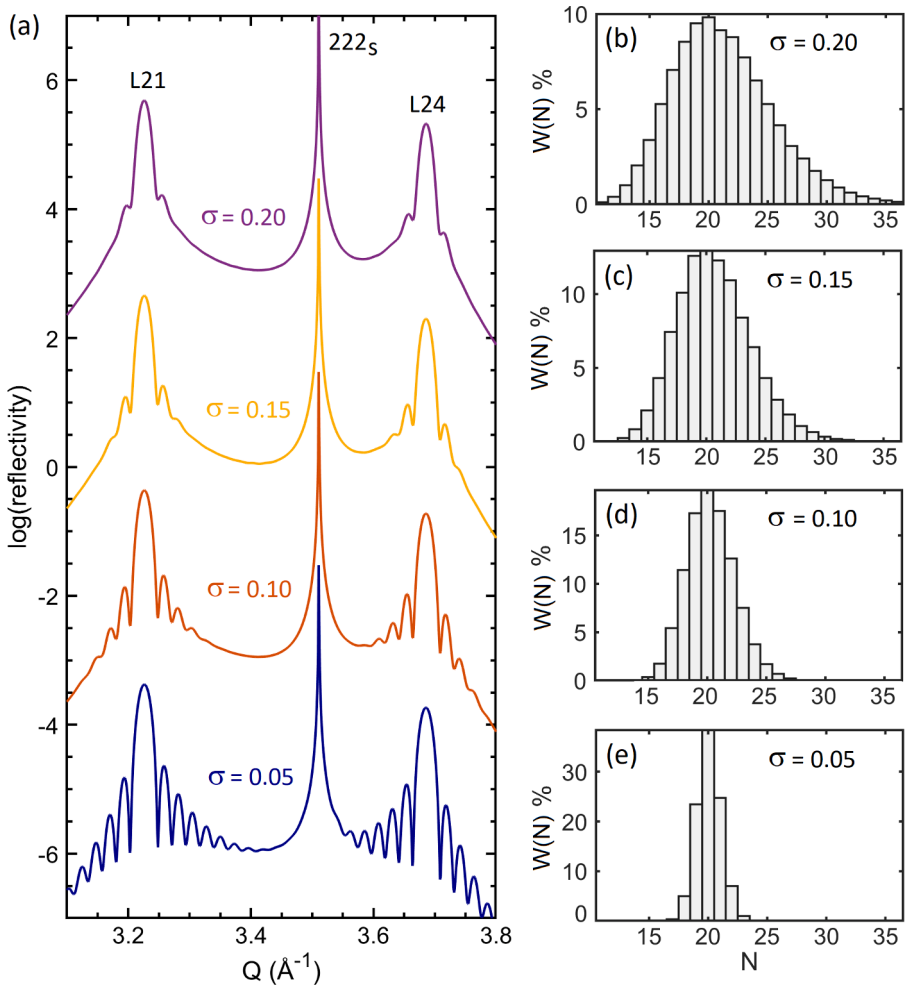

Fig. A3. (a) X-ray reflectivity simulation in $MnBi_2Te_4$ films on BaF_2 (111) substrate as a function of thickness distribution over the films. (b-e) Weight function $W(N)$ for intensity contribution of film regions with N SLs. The most probable number of SLs in the films is $N_0 = 20$ and the thickness deviation σ in Eq. (A.2) are indicated for each used function, as well as near the corresponding reflectivity curve.

is used to account for the intensity contribution of film areas containing N septuble layers.

$$L(x) = \frac{1}{x\sigma\sqrt{2\pi}}\exp\left[-\frac{\ln^2(x/b)}{2\sigma^2}\right] \tag{A.2}$$

where $b = N_0\exp(\sigma^2)$, N_0 is the most probable thickness (mode), and σ is the standard deviation in log scale. The simulated reflectivity curves in a Q range near the L24 peak are shown in Fig. A3(a) and the corresponding thickness distributions in Fig. A3(b–e). For films with most probable thickness around 20 SLs, the fringes vanish when the weights above 1% are distributed from $N = 13$ to 31 SLs.

A3. Reflection and transmission coefficients

An X-ray monochromatic plane-wave as it crosses an atomic plane undergoes reflection, refraction, and absorption. In standard kinematical theory of X-ray diffraction, only reflection is accounted for. On the other hand, the dynamical diffraction theory besides include these three phenomena, also takes into account the rescattering process between successive planes of atoms. In a more general approach, the dynamical diffraction theory can embrace more complex situations where many reflections are fully excited simultaneously, within the so-called multi-wave diffraction configuration [56,57]. However, for investigating Bragg reflections under specular diffraction geometry in layered materials, the theory can be significantly simplified in terms of the recursive series in Eq. (4) where the reflected and transmitted amplitudes of the X-ray waves by atomic monolayers (MLs) are given in terms of the reflection and transmission coefficients,

$$r_X = -i\frac{r_e\lambda C}{\sin\theta}\sum_a \eta_a f_a(Q,E) \quad \text{and} \quad t_X = 1 + i\frac{r_e\lambda}{\sin\theta}\sum_a \eta_a f_a(0,E)\,, \tag{A.3}$$

respectively. $Q = (4\pi/\lambda)\sin\theta$ is the modulus of the diffraction vector along the MLs normal direction given as a function of the incidence angle θ, scattering angle 2θ, and wavelength λ. η_a is the area density of atoms a in the ML plane and $f_a(Q,E) = f_a^0(Q) + f_a'(E) + if_a''(E)$ are their atomic scattering factors with resonant amplitudes $f_a'(E)$ and $f_a''(E)$ that are a function only of the X-ray photons of energy E. $r_e = 2.818 \times 10^{-5}$ Å is the classical electron

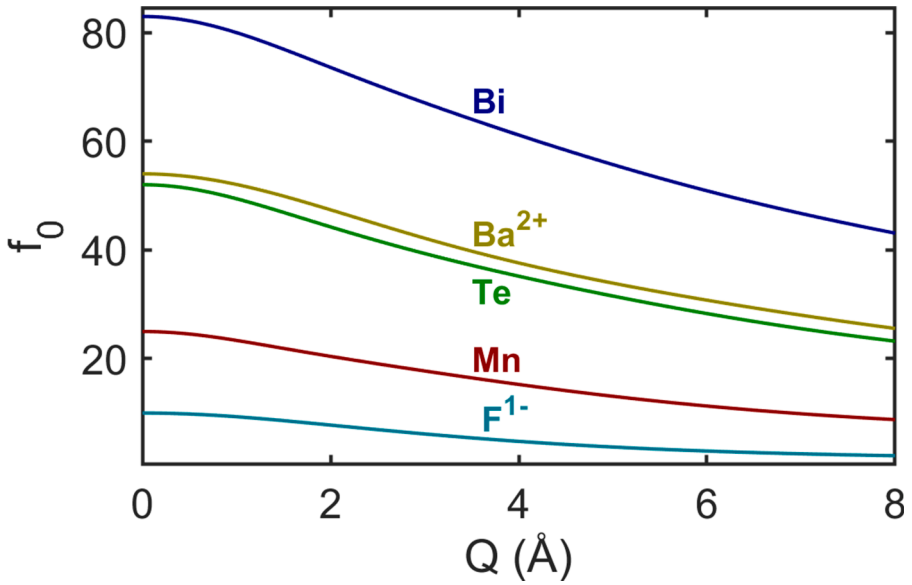

Fig. A4. Angle dependent component of atomic scattering amplitudes for X-rays $f_0(Q)$, given in number of electrons. Exact values were obtained from the `asfQ.m` codes [55].

Table A1
Resonant atomic scattering amplitues obtained from the `fpfpp.m` codes [55] for the used energy $E = 8041.57$ eV ($\lambda = 1.5418$ Å).

atom:	Mn	Bi	Te	Ba	F
f'_a =	− 0.532920	− 3.877040	− 0.153572	− 1.015625	+ 0.073181
f''_a =	+ 2.808637	+ 8.937114	+ 6.358851	+ 8.469466	+ 0.053438

radius from the Thomson elastic scattering and photoelectric absorption cross sections [58]. The $\sin\theta$ in the denominator of Eq. (A.3) takes into account area variation of the beam footprint at the sample surface, and the polarization term $C = \sqrt{(1+\cos^2 2\theta)/2}$ stands for unpolarized X-rays. Due to the collimating optics of the used diffractometer as well as the σ-polarization available in most synchrotron diffraction stations, $C = 1$ has been considered throughout this work.

From the perspective of the 00L film reflections and *hhh* substrate reflections, each ML contains only one type of chemical element, that is the MLs are monoatomic layers. Basically there are the Mn, Bi, and Te MLs in the film and the Ba^{2+} and F^{1-} MLs in the substrate. The actual values of non-resonant atomic scattering amplitudes $f_a^0(Q)$, are shown in Fig. A4 as a function only of Q within the spherosymmetric atom approximation [55]. No ionic charges were considered for the metallic atoms. Table A1 provides the resonant amplitudes values used in the X-ray diffraction simulations. For the area density of atoms in the MLs, η_a in Eq. (A.3), the used values where $\eta_{Ba} = \eta_F = 2/a_S \sin(60^\circ) = 6.0076 \times 10^{-2}$ atoms/Å^2 in the substrate MLs, $\eta_{Bi} = \eta_{Te} = 1/a_{QL}\sin(120^\circ) = 6.0025 \times 10^{-2}$ atoms/Å^2 in the QLs, and $\eta_{Mn} = \eta_{Bi} = \eta_{Te} = 1/a_{SL}\sin(120^\circ) = 6.1483 \times 10^{-2}$ atoms/Å^2 in the SLs.

References

[1] M.M. Otrokov, I.P. Rusinov, M. Blanco-Rey, M. Hoffmann, A.Y. Vyazovskaya, S. V. Eremeev, A. Ernst, P.M. Echenique, A. Arnau, E.V. Chulkov, Unique thickness-dependent properties of the van der Waals interlayer antiferromagnet $MnBi_2Te_4$ films, Phys. Rev. Lett. 122 (2019) 107202, https://doi.org/10.1103/PhysRevLett.122.107202.

[2] W. Mortelmans, S. De Gendt, M. Heyns, C. Merckling, Epitaxy of 2D chalcogenides: aspects and consequences of weak van der Waals coupling, Appl. Mater. Today 22 (2021) 100975, https://doi.org/10.1016/j.apmt.2021.100975.

[3] H. Li, C. Li, B. Tao, S. Gu, Y. Xie, H. Wu, G. Zhang, G. Wang, W. Zhang, H. Chang, Two-dimensional metal telluride atomic crystals: preparation, physical properties, and applications, Adv. Funct. Mater. (2021) 2010901, https://doi.org/10.1002/adfm.202010901.

[4] Y.L. Chen, J.G. Analytis, J.-H. Chu, Z.K. Liu, S.-K. Mo, X.L. Qi, H.J. Zhang, D.H. Lu, X. Dai, Z. Fang, S.C. Zhang, I.R. Fisher, Z. Hussain, Z.-X. Shen, Experimental realization of a three-dimensional topological insulator, Bi_2Te_3, Science 325 (2009) 178–181, https://doi.org/10.1126/science.1173034.

[5] H. Zhang, C.-X. Liu, X.-L. Qi, X. Dai, Z. Fang, S.-C. Zhang, Topological insulators in Bi_2Se_3, Bi_2Te_3 and Sb_2Te_3 with a single Dirac cone on the surface, Nat. Phys. 5 (2009) 438–442, https://doi.org/10.1038/nphys1270.

[6] Y. Xia, D. Qian, D. Hsieh, L. Wray, A. Pal, H. Lin, A. Bansil, D. Grauer, Y.S. Hor, R. J. Cava, M.Z. Hasan, Observation of a large-gap topological-insulator class with a single Dirac cone on the surface, Nat. Phys. 5 (2009) 398–402, https://doi.org/10.1038/nphys1274.

[7] D. Hsieh, Y. Xia, D. Qian, L. Wray, F. Meier, J.H. Dil, J. Osterwalder, L. Patthey, A. V. Fedorov, H. Lin, A. Bansil, D. Grauer, Y.S. Hor, R.J. Cava, M.Z. Hasan, Observation of time-reversal-protected single-dirac-cone topological-insulator states in Bi_2Te_3 and Sb_2Te_3, Phys. Rev. Lett. 103 (2009) 146401, https://doi.org/10.1103/PhysRevLett.103.146401.

[8] Y.-Y. Li, G. Wang, X.-G. Zhu, M.-H. Liu, C. Ye, X. Chen, Y.-Y. Wang, K. He, L.-L. Wang, X.-C. Ma, H.-J. Zhang, X. Dai, Z. Fang, X.-C. Xie, Y. Liu, X.-L. Qi, J.-F. Jia, S.-C. Zhang, Q.-K. Xue, Intrinsic topological insulator Bi_2Te_3 thin films on Si and their thickness limit, Adv. Mater. 22 (2010) 4002–4007, https://doi.org/10.1002/adma.201000368.

[9] G. Wang, X.-G. Zhu, Y.-Y. Sun, Y.-Y. Li, T. Zhang, J. Wen, X. Chen, K. He, L.-L. Wang, X.-C. Ma, J.-F. Jia, S.B. Zhang, Q.-K. Xue, Topological insulator thin films of Bi_2Te_3 with controlled electronic structure, Adv. Mater. 23 (2011) 2929–2932, https://doi.org/10.1002/adma.201100678.

[10] K. Hoefer, C. Becker, D. Rata, J. Swanson, P. Thalmeier, L.H. Tjeng, Intrinsic conduction through topological surface states of insulating Bi_2Te_3 epitaxial thin films, Proc. Natl. Acad. Sci. U.S.A. 111 (2014) 14979–14984, https://doi.org/10.1073/pnas.1410591111.

[11] Y. Guo, Z. Liu, H. Peng, A roadmap for controlled production of topological insulator nanostructures and thin films, Small 11 (2015) 3290–3305, https://doi.org/10.1002/smll.201403426.

[12] C.I. Fornari, P.H.O. Rappl, S.L. Morelhão, E. Abramof, Structural properties of Bi_2Te_3 topological insulator thin films grown by molecular beam epitaxy on (111) BaF_2 substrates, J. Appl. Phys. 119 (2016) 165303, https://doi.org/10.1063/1.4947266.

[13] S.L. Morelhão, S.W. Kycia, S. Netzke, C.I. Fornari, P.H.O. Rappl, E. Abramof, Dynamics of defects in van der Waals epitaxy of bismuth telluride topological insulators, J. Phys. Chem. C 123 (2019) 24818–24825, https://doi.org/10.1021/acs.jpcc.9b05377.

[14] C.I. Fornari, E. Abramof, P.H.O. Rappl, S.W. Kycia, S.L. Morelhão, Morphology control in van der Waals epitaxy of bismuth telluride topological insulators, MRS Adv. 5 (2020) 1891–1897, https://doi.org/10.1557/adv.2020.202.

[15] C.-Z. Chang, J. Zhang, X. Feng, J. Shen, Z. Zhang, M. Guo, K. Li, Y. Ou, P. Wei, L.-L. Wang, Z.-Q. Ji, Y. Feng, S. Ji, X. Chen, J. Jia, X. Dai, Z. Fang, S.-C. Zhang, K. He, Y. Wang, L. Lu, X.-C. Ma, Q.-K. Xue, Experimental observation of the quantum anomalous Hall effect in a magnetic topological insulator, Science 340 (2013) 167–170, https://doi.org/10.1126/science.1234414.

[16] C.-Z. Chang, W. Zhao, D.Y. Kim, H. Zhang, B.A. Assaf, D. Heiman, S.-C. Zhang, C. Liu, M.H.W. Chan, J.S. Moodera, High-precision realization of robust quantum anomalous Hall state in a hard ferromagnetic topological insulator, Nat. Mater. 14 (2015) 473–477, https://doi.org/10.1038/nmat4204.

[17] C.I. Fornari, H. Bentmann, S.L. Morelhão, T.R.F. Peixoto, P.H.O. Rappl, A.-V. Tcakaev, V. Zabolotnyy, M. Kamp, T.-L. Lee, C.-H. Min, P. Kagerer, R.C. Vidal, A. Isaeva, M. Ruck, V. Hinkov, F. Reinert, E. Abramof, Incorporation of europium in Bi_2Te_3 topological insulator epitaxial films, J. Phys. Chem. C 124 (2020) 16048–16057, https://doi.org/10.1021/acs.jpcc.0c05077.

[18] A.I. Figueroa, S.E. Harrison, L.J. Collins-McIntyre, G. van der Laan, T. Hesjedal, Magnetic ordering in Ho-doped Bi_2Te_3 topological insulator, Phys. Status Solidi RRL 10 (2016) 467–470, https://doi.org/10.1002/pssr.201600061.

[19] S.E. Harrison, L.J. Collins-McIntyre, P. Schönherr, A. Vailionis, V. Srot, P.A. van Aken, A.J. Kellock, A. Pushp, S.S.P. Parkin, J.S. Harris, B. Zhou, Y.L. Chen, T. Hesjedal, Massive Dirac fermion observed in lanthanide-doped topological insulator thin films, Sci. Rep. 5 (2015) 15767, https://doi.org/10.1038/srep15767.

[20] M.M. Otrokov, I.I. Klimovskikh, H. Bentmann, D. Estyunin, A. Zeugner, Z.S. Aliev, S. Gaß, A.U.B. Wolter, A.V. Koroleva, A.M. Shikin, M. Blanco-Rey, M. Hoffmann, I. P. Rusinov, A.Y. Vyazovskaya, S.V. Eremeev, Y.M. Koroteev, V.M. Kuznetsov, F. Freyse, J. Sánchez-Barriga, I.R. Amiraslanov, M.B. Babanly, N.T. Mamedov, N. A. Abdullayev, V.N. Zverev, A. Alfonsov, V. Kataev, B. Büchner, E.F. Schwier, S. Kumar, A. Kimura, L. Petaccia, G. Di Santo, R.C. Vidal, S. Schatz, K. Kißner, M. ünzelmann, C.H. Min, S. Moser, T.R.F. Peixoto, F. Reinert, A. Ernst, P. M. Echenique, A. Isaeva, E.V. Chulkov, Prediction and observation of an antiferromagnetic topological insulator, Nature 576 (2019) 416–422, https://doi.org/10.1038/s41586-019-1840-9.

[21] J. Li, Y. Li, S. Du, Z. Wang, B.-L. Gu, S.-C. Zhang, K. He, W. Duan, Y. Xu, Intrinsic magnetic topological insulators in van der Waals layered $MnBi_2Te_4$-family materials, Sci. Adv. 5 (2019), https://doi.org/10.1126/sciadv.aaw5685.

[22] J.W.G. Bos, H.W. Zandbergen, M.-H. Lee, N.P. Ong, R.J. Cava, Structures and thermoelectric properties of the infinitely adaptive series $(Bi_2)_m(Bi_2Te_3)_n$, Phys. Rev. B 75 (2007) 195203, https://doi.org/10.1103/PhysRevB.75.195203.

[23] H. Steiner, V. Volobuev, O. Caha, G. Bauer, G. Springholz, V. Holý, Structure and composition of bismuth telluride topological insulators grown by molecular beam epitaxy, J. Appl. Cryst. 47 (2014) 1889–1900, https://doi.org/10.1107/S1600576714020445.

[24] Z.S. Aliev, I.R. Amiraslanov, D.I. Nasonova, A.V. Shevelkov, N.A. Abdullayev, Z. A. Jahangirli, E.N. Orujlu, M.M. Otrokov, N.T. Mamedov, M.B. Babanly, E. V. Chulkov, Novel ternary layered manganese bismuth tellurides of the MnTe-Bi_2Te_3 system: synthesis and crystal structure, J. Alloys Compd. 789 (2019) 443–450, https://doi.org/10.1016/j.jallcom.2019.03.030.

[25] E.D.L. Rienks, S. Wimmer, J. Sánchez-Barriga, O. Caha, P.S. Mandal, J. Růžička, A. Ney, H. Steiner, V.V. Volobuev, H. Groiss, M. Albu, G. Kothleitner, J. Michalička, S.A. Khan, J. Minár, H. Ebert, G. Bauer, F. Freyse, A. Varykhalov, O. Rader, G. Springholz, Large magnetic gap at the Dirac point in Bi_2Te_3/ $MnBi_2Te_4$ heterostructures, Nature 576 (2019) 423–428, https://doi.org/10.1038/s41586-019-1826-7.

[26] P. Kagerer, C.I. Fornari, S. Buchberger, S.L. Morelhão, R.C. Vidal, A. Tcakaev, V. Zabolotnyy, E. Weschke, V. Hinkov, M. Kamp, B. Büchner, A. Isaeva, H. Bentmann, F. Reinert, Molecular beam epitaxy of antiferromagnetic $(MnBi_2Te_4)(Bi_2Te_4)$ thin films on BaF_2 (111), J. Appl. Phys. 128 (2020) 135303, https://doi.org/10.1063/5.0025933.

[27] J. Lapano, L. Nuckols, A.R. Mazza, Y.-Y. Pai, J. Zhang, B. Lawrie, R.G. Moore, G. Eres, H.N. Lee, M.-H. Du, T.Z. Ward, J.S. Lee, W.J. Weber, Y. Zhang, M. Brahlek, Adsorption-controlled growth of $MnTe(Bi_2Te_3)_n$ by molecular beam epitaxy exhibiting stoichiometry-controlled magnetism, Phys. Rev. Mater 4 (2020) 111201, https://doi.org/10.1103/PhysRevMaterials.4.111201.

[28] R.C. Vidal, A. Zeugner, J.I. Facio, R. Ray, M.H. Haghighi, A.U.B. Wolter, L. T. Corredor Bohorquez, F. Caglieris, S. Moser, T. Figgemeier, T.R.F. Peixoto, H. B. Vasili, M. Valvidares, S. Jung, C. Cacho, A. Alfonsov, K. Mehlawat, V. Kataev, C. Hess, M. Richter, B. Büchner, J. van den Brink, M. Ruck, F. Reinert, H. Bentmann, A. Isaeva, Topological electronic structure and intrinsic magnetization in $MnBi_4Te_7$: aBi_2Te_3 derivative with a periodic Mn sublattice, Phys. Rev. X 9 (2019) 041065, https://doi.org/10.1103/PhysRevX.9.041065.

[29] S.L. Morelhão, G.E.S. Brito, E. Abramof, Nanostructure of sol–gel films by X-ray specular reflectivity, Appl. Phys. Lett. 80 (2002) 407–409, https://doi.org/10.1063/1.1436271.

[30] J.-Q. Yan, Q. Zhang, T. Heitmann, Z. Huang, K.Y. Chen, J.-G. Cheng, W. Wu, D. Vaknin, B.C. Sales, R.J. McQueeney, Crystal growth and magnetic structure of $MnBi_2Te_4$, Phys. Rev. Mater. 3 (2019) 064202, https://doi.org/10.1103/PhysRevMaterials.3.064202.

[31] A.K. Geim, I.V. Grigorieva, Van der Waals heterostructures, Nature 499 (2013) 419–425, https://doi.org/10.1038/nature12385.

[32] P.A. Vermeulen, J. Mulder, J. Momand, B.J. Kooi, Strain engineering of van der Waals heterostructures, Nanoscale 10 (2018) 1474–1480, https://doi.org/10.1039/C7NR07607J.

[33] J.A. Hagmann, X. Li, S. Chowdhury, S.-N. Dong, S. Rouvimov, S.J. Pookpanratana, K.M. Yu, T.A. Orlova, T.B. Bolin, C.U. Segre, D.G. Seiler, C.A. Richter, X. Liu, M. Dobrowolska, J.K. Furdyna, Molecular beam epitaxy growth and structure of self-assembled Bi_2Se_3/Bi_2MnSe_4 multilayer heterostructures, New J. Phys. 19 (2017) 085002, https://doi.org/10.1088/1367-2630/aa759c.

[34] G. Springholz, S. Wimmer, H. Groiss, M. Albu, F. Hofer, O. Caha, D. Kriegner, J. Stangl, G. Bauer, V. Holý, Structural disorder of natural Bi_mSe_n superlattices grown by molecular beam epitaxy, Phys. Rev. Mater. 2 (2018) 054202, https://doi.org/10.1103/PhysRevMaterials.2.054202.

[35] M. Idrees, H.U. Din, S.A. Khan, I. Ahmad, L.-Y. Gan, C.V. Nguyen, B. Amin, Van der Waals heterostructures of P, BSe, and SiC monolayers, J. Appl. Phys. 125 (2019) 094301, https://doi.org/10.1063/1.5082884.

[36] S.L. Morelhão, C.I. Fornari, P.H.O. Rappl, E. Abramof, Nanoscale characterization of bismuth telluride epitaxial layers by advanced X-ray analysis, J. Appl. Cryst. 50 (2017) 399–410, https://doi.org/10.1107/S1600576717000760.

[37] S.L. Morelhão, S. Kycia, Enhanced X-ray phase determination by three-beam diffraction, Phys. Rev. Lett. 89 (2002) 015501, https://doi.org/10.1103/PhysRevLett.89.015501.

[38] D.S. Lee, T.-H. Kim, C.-H. Park, C.-Y. Chung, Y.S. Lim, W.-S. Seo, H.-H. Park, Crystal structure, properties and nanostructuring of a new layered chalcogenide semiconductor, Bi_2MnTe_4, CrystEngComm 15 (2013) 5532–5538, https://doi.org/10.1039/C3CE40643A.

[39] S. Nakajima, The crystal structure of $Bi_2Te_{3-x}Se_x$, J. Phys. Chem. Solids 24 (1963) 479–485, https://doi.org/10.1016/0022-3697(63)90207-5.

[40] T. Hirahara, M.M. Otrokov, T.T. Sasaki, K. Sumida, Y. Tomohiro, S. Kusaka, Y. Okuyama, S. Ichinokura, M. Kobayashi, Y. Takeda, K. Amemiya, T. Shirasawa, S. Ideta, K. Miyamoto, K. Tanaka, S. Kuroda, T. Okuda, K. Hono, S.V. Eremeev, E. V. Chulkov, Fabrication of a novel magnetic topological heterostructure and temperature evolution of its massive Dirac cone, Nat. Commun. 11 (2020) 4821, https://doi.org/10.1038/s41467-020-18645-9.

[41] N. Bouad, L. Chapon, R.-M. Marin-Ayral, F. Bouree-Vigneron, J.-C. Tedenac, Neutron powder diffraction study of strain and crystallite size in mechanically alloyed PbTe, J. Solid State Chem. 173 (2003) 189–195, https://doi.org/10.1016/S0022-4596(03)00017-3.

[42] H. Franzen, C. Sterner, The X-ray photoelectron spectra of MnS, MnSe, and MnTe, J. Solid State Chem. 25 (1978) 227–230, https://doi.org/10.1016/0022-4596(78)90107-X.

[43] T.P. Ginley, Y. Wang, S. Law, Topological insulator film growth by molecular beam epitaxy: a review, Crystals 6 (2016) 154, https://doi.org/10.3390/cryst6110154.

[44] L.A. Walsh, C.L. Hinkle, Van der Waals epitaxy: 2D materials and topological insulators, Appl. Mater. Today 9 (2017) 504–515, https://doi.org/10.1016/j.apmt.2017.09.010.

[45] A. Ghasemi, D. Kepaptsoglou, P.L. Galindo, Q.M. Ramasse, T. Hesjedal, V. K. Lazarov, Van der Waals epitaxy between the highly lattice mismatched Cu-doped FeSe and Bi_2Te_3, NPG Asia Mater. 9 (2017) e402, https://doi.org/10.1038/am.2017.111.

[46] S.L. Morelhão, S. Kycia, S. Netzke, C.I. Fornari, P.H.O. Rappl, E. Abramof, Hybrid reflections from multiple X-ray scattering in epitaxial bismuth telluride topological insulator films, Appl. Phys. Lett. 112 (2018) 101903, https://doi.org/10.1063/1.5020375.

[47] S.L. Morelhão, G.E.S. Brito, E. Abramof, Characterization of erbium oxide sol-gel films and devices by grazing incidence X-ray reflectivity, J. Alloys Compd. 344 (2002) 207–211, https://doi.org/10.1016/S0925-8388(02)00342-0.

[48] S.L. Morelhão, C.I. Fornari, P.H.O. Rappl, E. Abramof, Nanoscale characterization of bismuth telluride eepitaxial layers by advanced X-ray analysis, J. Appl. Cryst. 50 (2017) 399–410, https://doi.org/10.1107/S1600576717000760.

[49] S.L. Morelhão, L. Cardoso, Simulation of hybrid reflections in X-ray multiple diffraction experiments, J. Cryst. Growth 110 (1991) 543–552, https://doi.org/10.1016/0022-0248(91)90291-C.

[50] L.H. Avanci, M.A. Hayashi, L.P. Cardoso, S.L. Morelhão, F. Riesz, K. Rakennus, T. Hakkarainen, Mapping of Bragg-surface diffraction of InP/GaAs(100) structure, J. Cryst. Growth 188 (1998) 220–224, https://doi.org/10.1016/S0022-0248(98)00074-8.

[51] S.L. Morelhão, A.A. Quivy, J. Härtwig, Hybrid and effective satellites for studying superlattices, Microelectr. J. 34 (2003) 695–699, https://doi.org/10.1016/S0026-2692(03)00101-0.

[52] A. Antunes, A.M.V. Safatle, P.S.M. Barros, S.L. Morelhão, X-ray imaging in advanced studies of ophthalmic diseases, Med. Phys. 33 (2006) 2338–2343, https://doi.org/10.1118/1.2207135.

[53] A.S. de Menezes, A.O. dos Santos, J.M.A. Almeida, J.R.R. Bortoleto, M.A. Cotta, S. L. Morelhão, L.P. Cardoso, Direct observation of tetragonal distortion in epitaxial structures through secondary peak split in a synchrotron radiation renninger scan, Cryst. Growth Des. 10 (2010) 3436–3441, https://doi.org/10.1021/cg100146x.
[54] S.L. Morelhão, C.M.R. Remédios, R.O. Freitas, A.O. dos Santos, X-ray phase measurements as a probe of small structural changes in doped nonlinear optical crystals, J. Appl. Cryst. 44 (2011) 93–101, https://doi.org/10.1107/S0021889810042391.
[55] S.L. Morelhão, Computer Simulation Tools for X-ray Analysis, Springer International Publishing, Cham, 2016, https://doi.org/10.1007/978-3-319-19554-4.
[56] E. Weckert, K. Hümmer, Multiple-Beam X-ray diffraction for physical determination of reflection phases and its applications, Acta Cryst. A 53 (1997) 108–143, https://doi.org/10.1107/S0108767396011117.
[57] S.L. Morelhão, C.M.R. Remédios, G.A. Calligaris, G. Nisbet, X-ray dynamical diffraction in amino acid crystals: a step towards improving structural resolution of biological molecules via physical phase measurements, J. Appl. Cryst. 50 (2017) 689–700, https://doi.org/10.1107/S1600576717004757.
[58] J. Als-Nielsen, D. McMorrow, X-rays and Their Interaction with Matter, John Wiley & Sons, Ltd, 2011, pp. 1–28.